JSS Focus Issue on Atomic Layer Etching and Cleaning

Atomic Layer Etching of HfO_2 Using Sequential, Self-Limiting Thermal Reactions with $Sn(acac)_2$ and HF

Younghee Lee,[a] Jaime W. DuMont,[a] and Steven M. George[a,b,z]

[a]*Department of Chemistry and Biochemistry, University of Colorado at Boulder, Colorado 80309, USA*
[b]*Department of Mechanical Engineering, University of Colorado at Boulder, Colorado 80309, USA*

The atomic layer etching (ALEt) of HfO_2 was performed using sequential, self-limiting thermal reactions with tin(II) acetylacetonate ($Sn(acac)_2$) and HF as the reactants. The HF source was a HF-pyridine solution. The etching of HfO_2 was linear with atomic level control versus number of $Sn(acac)_2$ and HF reaction cycles. The HfO_2 ALEt was measured at temperatures from 150–250°C. Quartz crystal microbalance (QCM) measurements determined that the mass change per cycle (MCPC) increased with temperature from −6.7 ng/(cm^2 cycle) at 150°C to −11.2 ng/(cm^2 cycle) at 250°C. These MCPC values correspond to etch rates from 0.070 Å/cycle at 150°C to 0.117 Å/cycle at 250°C. X-ray reflectivity analysis confirmed the linear removal of HfO_2 and measured an HfO_2 ALEt etch rate of 0.11 Å/cycle at 200°C. Fourier transform infrared (FTIR) spectroscopy measurements also observed HfO_2 ALEt using the infrared absorbance of the Hf-O stretching vibration. FTIR analysis also revealed absorbance features consistent with HfF_4 or HfF_x surface species as a reaction intermediate. The HfO_2 etching is believed to follow the reaction: $HfO_2 + 4Sn(acac)_2 + 4HF \rightarrow Hf(acac)_4 + 4SnF(acac) + 2H_2O$. In the proposed reaction mechanism, $Sn(acac)_2$ donates acac to the substrate to produce $Hf(acac)_4$. HF allows SnF(acac) and H_2O to leave as reaction products. The thermal ALEt of many other metal oxides, as well as metal nitrides, phosphides, sulfides and arsenides, should be possible by a similar mechanism.
 [DOI: 10.1149/2.0041506jss]

Manuscript submitted December 30, 2014; revised manuscript received February 26, 2015. Published March 12, 2015. *This paper is part of the JSS Focus Issue on Atomic Layer Etching and Cleaning.*

Atomic layer etching (ALEt) is a thin film removal technique based on sequential, self-limiting surface reactions.[1–3] ALEt can be viewed as the reverse of atomic layer deposition (ALD).[4] ALEt is able to remove thin films with atomic layer control. ALD and ALEt are able to provide the necessary processing techniques for surface engineering at the atomic level.[5,6] This atomic level control is needed for the nanofabrication of a wide range of nanoscale devices.[7]

Until recently, ALEt processes have been reported using only ion-enhanced or energetic noble gas atom-enhanced surface reactions.[1–3] In these ALEt processes, a halogen is adsorbed on the surface of the material. Subsequently, ion or noble gas atom bombardment is used to desorb halogen compounds that etch the material. Using this approach, ALEt has been reported for Si,[2,3,8–12] Ge,[6,13] and compound semiconductors.[14–17] ALEt has also been demonstrated for a variety of metal oxides.[7,18–20] Additional ALEt studies have been conducted on various carbon substrates.[21–23]

The ALEt of Al_2O_3 was recently reported using sequential, self-limiting thermal reactions with $Sn(acac)_2$ and HF as the reactants.[24] The linear removal of Al_2O_3 was observed at temperatures from 150–250°C without the use of ion or noble gas atom bombardment. Al_2O_3 ALEt etch rates varied with temperature from 0.14 Å/cycle at 150°C to 0.61 Å/cycle at 250°C.[24] The $Sn(acac)_2$ and HF thermal reactions were both self-limiting versus reactant exposure. In addition, the Al_2O_3 films were smoothed by Al_2O_3 ALEt cycles.[24] The overall Al_2O_3 etching reaction was proposed to be: $Al_2O_3 + 6Sn(acac)_2 + 6HF \rightarrow 2Al(acac)_3 + 6SnF(acac) + 3H_2O$.[24]

HfO_2 is an important high k dielectric material that is a replacement for SiO_2 in gate oxides in metal oxide semiconductor field effect transistors (MOSFET).[25,26] The HfO_2 films used in the gate stack have been grown using ALD.[27] The HfO_2-based gate oxide was introduced in 2007 for the 45 nm node in complementary MOSFET technology.[28] HfO_2 is also being employed as the gate dielectric in FinFET structures.[29,30] Etching of HfO_2 films may be needed to define the gate dielectric thickness.[7] To meet these needs, HfO_2 ALEt has been previously developed using BCl_3 to adsorb chlorine on the HfO_2 substrate and then energetic Ar beams to desorb Cl-containing compounds that etch the HfO_2 material.[7]

In this study, a new approach for HfO_2 ALEt is demonstrated using sequential, self-limiting thermal reactions with $Sn(acac)_2$ and HF as the reactants. Quartz crystal microbalance (QCM) measurements are used to study HfO_2 ALEt. The QCM analysis obtains the HfO_2 etch rates and the mass changes after individual $Sn(acac)_2$ and HF exposures. The mass change per cycle (MCPC) and the individual mass changes during the $Sn(acac)_2$ and HF exposures are used to develop a mechanism for HfO_2 ALEt. In addition, Fourier transform infrared (FTIR) analysis is able to monitor HfO_2 ALEt and characterize the $Sn(acac)_2$ and HF reaction products on the surface. This new approach for HfO_2 ALEt offers an alternative and may have advantages relative to ALEt methods based on ions or energetic neutrals.

Experimental

Viscous flow reactor equipped for in situ QCM measurements.— The ALEt reactions were performed in a viscous flow ALD reactor.[31] The reaction temperatures varied from 150–250°C. A proportional-integral-derivative (PID) temperature controller (2604, Eurotherm) maintained the temperature to within ±0.04°C. The pressure was measured in the reactor using a capacitance manometer (Baratron 121A, MKS). The ALD reactor was equipped with an in situ quartz crystal microbalance (QCM).[31] An RC-cut quartz crystal[32] (gold coated and polished, 6 MHz, Colnatec) was positioned in a sensor head (BSH-150, Inficon). The sensor head was then sealed with high temperature epoxy (Epo-Tek H21D, Epoxy technology). A thin film deposition monitor (Maxtek TM-400, Inficon) was used to record the QCM measurements.

Sequential exposure of tin(II) acetylacetonate ($Sn(acac)_2$, 37–38% Sn, Gelest) and HF-pyridine (70 wt% HF, Sigma-Aldrich) were employed for the HfO_2 ALEt reactions. These precursors are shown in Figure 1. Use of gaseous HF from HF-pyridine enables the safe handling of anhydrous HF. HF-pyridine is a liquid at room temperature and is known as Olah's reagent.[33] The HF-pyridine solution has an equilibrium with gaseous HF. Our mass spectrometer analysis has shown that HF dominates the vapor pressure of HF-pyridine. Our

[z]E-mail: steven.george@colorado.edu

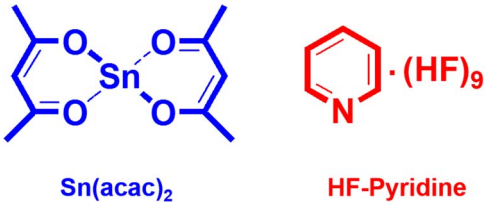

Figure 1. Pictures of $Sn(acac)_2$ and HF-pyridine precursors.

measurement of the HF pressure over the HF-pyridine solution was 90–100 Torr at room temperature.

$Sn(acac)_2$ and HF-pyridine were transferred to stainless steel bubblers in a dry N_2-filled glove bag. The bubbler containing the HF-pyridine was electrochemically coated with gold to prevent HF reaction with the stainless steel. The $Sn(acac)_2$ precursor was held at 100°C to produce a vapor pressure of 15–20 mTorr. The HF-pyridine precursor was maintained at room temperature. The HfO_2 films were grown by HfO_2 ALD using tetrakisdimethylamido hafnium (TDMAH) (≥99.99%, Sigma-Aldrich) and H_2O (Chromasolv for HPLC, Sigma-Aldrich). For the QCM experiments, the HfO_2 ALD films were grown at the same temperature as the HfO_2 ALEt experiments. TDMAH was transferred to a stainless steel bubbler and maintained at 67°C to produce a vapor pressure of 20 mTorr. The H_2O precursor was held at room temperature.

A mechanical pump (Pascal 2015SD, Alcatel) was used to pump the reactor. A constant total flow of 150 sccm of ultra high purity (UHP) N_2 carrier gas into the reactor was provided by three separate mass flow controllers (Type 1179A, MKS). Additional N_2 gas flow of 20 sccm was provided using a metering bellows-sealed valve (SS-4BMG, Swagelok) to prevent deposition on the backside of the QCM crystal.[31] A base pressure of ∼1 Torr in the reactor was produced by the total N_2 gas flow of 170 sccm.

Si wafers, X-ray reflectivity, X-ray photoelectron spectroscopy and spectroscopic ellipsometry.— The X-ray reflectivity (XRR), X-ray photoelectron spectroscopy (XPS) and spectroscopic ellipsometry (SE) experiments were performed on boron-doped Si (100) wafers (p-type, Silicon Valley Microelectronics). These wafers were cut into samples with dimensions of 2.5 cm by 2.5 cm. These substrates were used for HfO_2 ALD deposition at 200°C and then for subsequent HfO_2 ALEt experiments. Prior to HfO_2 ALD, the Si wafers were rinsed with acetone, isopropanol, and deionized water and then dried with UHP N_2 gas.

The ex situ XRR scans were recorded using a high resolution X-ray diffractometer (Bede D1, Jordan Valley Semiconductors) employing Cu Kα ($\lambda = 1.540$ Å) radiation. The filament voltage and current in the X-ray tube were 40 kV and 35 mA, respectively. A 10 arcsec step size and a 5 s acquisition time were used for recording all XRR scans with a range of 300 to 6000 arcsec. The analysis software (Bede REFS, Jordan Valley Semiconductors) fitted the XRR scans to determine film thickness, film density and surface roughness.

X-ray photoemission spectroscopy (XPS) analysis was performed using a PHI 5600 X-ray photoelectron spectrometer using a monochromatic Al Kα source. The XPS data were collected using Auger Scan (RBD Instruments). The XPS data were analyzed in CASA XPS (Casa Software Ltd.).

SE analysis determined the film thicknesses and refractive index. The measurement of Ψ and Δ were recorded using a spectroscopic ellipsometer (M-2000, J. A. Woollam) with a spectral range of 240 to 1700 nm and an incidence angle of 75°. The analysis software (CompleteEASE, J. A. Woollam) fitted Ψ and Δ based on a Sellmeier model to determine the thicknesses and refractive index of the film.[34]

FTIR spectroscopy measurements.— The in situ transmission FTIR measurements of HfO_2 ALEt were performed in a reactor equipped with an FTIR spectrometer.[35] The FTIR spectrometer (Nicolet 6700 FTIR from Thermo Scientific) utilized a high-sensitivity liquid-N_2-cooled mercury cadmium telluride (MCT-B) detector. The spectrometer, mirror, and detector were purged with dry, CO_2-free air. A total of 100 scans at 4 cm^{-1} resolution from 400 to 4000 cm^{-1} were recorded for each collected spectrum.

The transmission FTIR measurements were performed on high surface area SiO_2 nanoparticles (99.5%, US Research Nanomaterials Inc.) with an average diameter of 15–20 nm. The high surface area of these particles improved the signal-to-noise ratio compared with a flat sample.[36] Sample preparation involved pressing the SiO_2 nanoparticles into a tungsten grid support (Tech-Etch).[36,37] The tungsten grids were 2 × 3 cm^2. Each grid was 50 μm thick with 100 grid lines per inch.

The tungsten grid could be resistively heated using a DC power supply (6268B, 20V/20A, Hewlett-Packard). The voltage output of the power supply was controlled by a PID temperature controller (Love Controls 16B, Dwyer Instruments, Inc.). A type K thermocouple was attached to the bottom of the tungsten grid with Epoxy (Ceramabond 571, Aremco) that served to attach and electrically isolate the thermocouple during the experiment.

The HfO_2 films were grown with HfO_2 ALD using TDMAH and H_2O at 200°C. The HfO_2 ALEt reactions were performed using sequential exposures of $Sn(acac)_2$ and HF. Static dosing of both the ALD and ALEt precursors was utilized to achieve self-limiting behavior on the high surface area SiO_2 particles. During HfO_2 ALD, each TDMAH exposure consisted of a ∼1.0 Torr static dose for 30 s followed by a 240 s purge. For the H_2O reaction, each exposure consisted of a ∼1.0 Torr static dose for 30 s followed by a 240 s purge.

During HfO_2 ALEt, each $Sn(acac)_2$ exposure consisted of a ∼1.0 Torr static dose for 30 s followed by a 240 s purge. For the HF reaction, each HF exposure consisted of a ∼1.0 Torr static dose for 30 s followed by a 240 s purge. For these FTIR experiments, the HF-pyridine and H_2O precursors were maintained at room temperature. The stainless steel bubbler containing $Sn(acac)_2$ was held at 100°C. The stainless steel bubbler containing TDMAH was held at 70°C.

HfF_4 films were deposited using HfF_4 ALD with sequential exposures of TDMAH and HF at 150°C. The HfF_4 films were grown on a fresh HfO_2 ALD film that was prepared using three HfO_2 ALD cycles with TDMAH and H_2O as the reactants. Static dosing of the reactants was utilized to achieve self-limiting behavior of the surface reactions on the high surface area SiO_2 particles. During HfF_4 ALD, each TDMAH exposure consisted of a ∼1.0 Torr static dose for 30 s followed by a 240 s purge. Each HF exposure consisted of a ∼1.0 Torr static dose for 30 s followed by a 240 s purge.

Results and Discussion

QCM measurements.— Figure 2 displays the mass change during 100 ALEt cycles of sequential $Sn(acac)_2$ and HF reactions on an

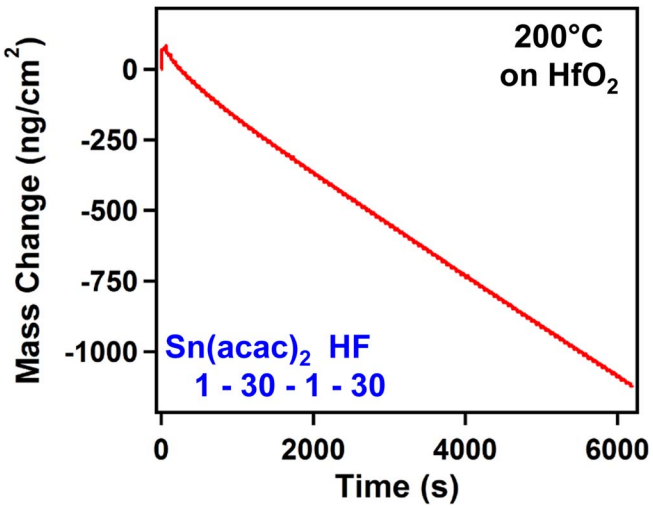

Figure 2. Mass change versus time for HfO_2 ALEt using sequential $Sn(acac)_2$ and HF exposures at 200°C.

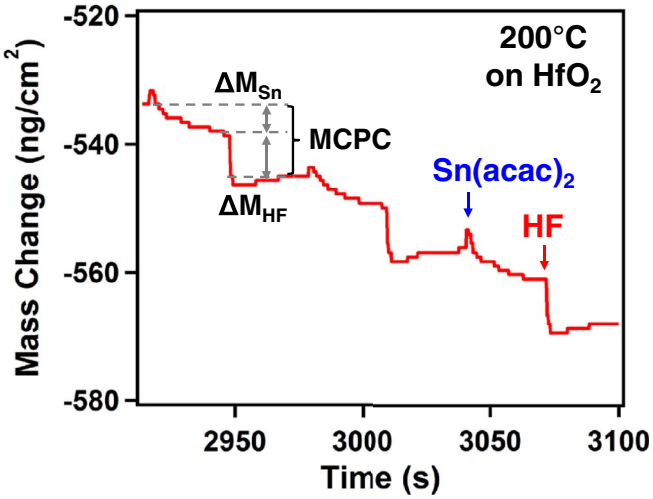

Figure 3. Expansion of linear region of Figure 2 showing the individual mass changes during the sequential $Sn(acac)_2$ and HF exposures at 200°C.

HfO_2 surface at 200°C. The initial HfO_2 film on the QCM sensor was deposited using 100 cycles of HfO_2 ALD with TDMAH and H_2O as the reactants at 200°C. One ALEt cycle was defined by a $Sn(acac)_2$ dose of 1.0 s, a N_2 purge of 30 s, a HF dose of 1.0 s, and a second N_2 purge of 30 s. This reaction sequence is designated as 1-30-1-30. The pressure transients during the $Sn(acac)_2$ and HF exposures were 20 mTorr and 80 mTorr, respectively.

The etching of the HfO_2 film in Figure 2 is linear and is consistent with a mass change per cycle (MCPC) = −11.1 ng/(cm^2 cycle). This MCPC corresponds to an etch rate of 0.116 Å/cycle based on the HfO_2 ALD film density of 9.6 g/cm^3 that was measured by XRR analysis. All of the ALEt cycles display a mass loss as a result of etching the HfO_2 film except during the first ALEt cycle. The first cycle shows mass gains of $\Delta M_{Sn} = 71$ ng/cm^2 and $\Delta M_{HF} = 6$ ng/cm^2.

The mass gain for ΔM_{Sn} on the first cycle is assigned to $Sn(acac)_2$ adsorption on the HfO_2 surface. The $Sn(acac)_2$ could either adsorb associatively as $Sn(acac)_2$* or dissociatively as Sn(acac)* and (acac)*. The asterisks designate a surface species. The mass gain for ΔM_{HF} on the first cycle is explained by HF adsorption or the formation of HfF_4 or HfF_x species by the reaction of HF with the underlying HfO_2 surface. The reaction $HfO_2 + 4HF \rightarrow HfF_4 + 2H_2O$ is spontaneous with $\Delta G = -19$ kcal at 200°C.[38] This first cycle establishes the initial $Sn(acac)_2$ and HF, HfF_4 or HfF_x species on the HfO_2 substrate.

Figure 3 displays an enlargement of the mass changes versus time at 200°C for three cycles in the steady state linear etching regime in Figure 2. There is a gradual mass decrease after a small mass gain coinciding with the $Sn(acac)_2$ exposure. This behavior suggests $Sn(acac)_2$ adsorption followed by either $Sn(acac)_2$ desorption and/or the removal of reaction products. A mass change of $\Delta M_{Sn} = -4.8$ ng/cm^2 was observed after 1.0 s of $Sn(acac)_2$ exposure. A mass change of $\Delta M_{HF} = -6.3$ ng/cm^2 was observed after 1.0 s of HF exposure. The experimental variation of these mass changes was measured over 50 HfO_2 ALEt cycles. The standard deviation on the ΔM_{Sn} and ΔM_{HF} mass changes was <0.1 ng/cm^2.

Figure 4 shows the MCPC and the ΔM_{Sn}/MCPC ratio during 100 cycles of HfO_2 ALEt at 200°C. The MCPC is defined by MCPC = $\Delta M_{Sn} + \Delta M_{HF}$. The standard deviation on the MCPC was also <0.1 ng/cm^2. Figure 4a displays ΔM_{Sn}, ΔM_{HF} and MCPC for the same 100 cycles of HfO_2 ALEt on the HfO_2 film at 200°C as shown in Figure 2. The MCPC varies from −26 ng/(cm^2 cycle) to −17 ng/(cm^2 cycle) over the second to fifth ALEt cycles. The MCPC decreases to a steady-state value of −11.1 ng/(cm^2 cycle) after ∼20 HfO_2 ALEt cycles. These first 20 HfO_2 ALEt cycles prior to reaching the steady state values define the nucleation regime.

Figure 4b displays the ΔM_{Sn}/MCPC ratio during the same 100 cycles as shown in Figure 4a. This ΔM_{Sn} /MCPC ratio varies from

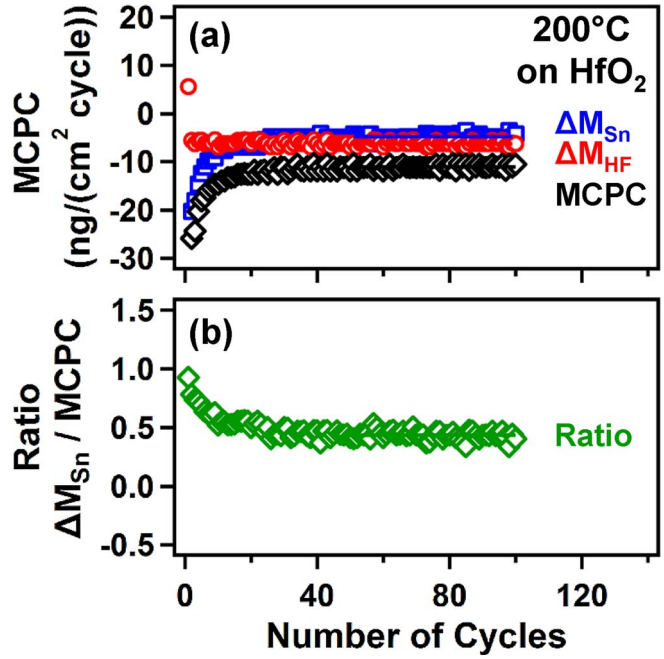

Figure 4. (a) Mass change after the $Sn(acac)_2$ exposure (ΔM_{Sn}), mass change after the HF exposure (ΔM_{HF}) and mass change per cycle (MCPC) versus number of ALEt cycles at 200°C. (b) ΔM_{Sn}/MCPC ratio versus number of ALEt cycles.

0.78 to 0.64 over the second to fifth ALEt cycles. The ratio then slowly decreases to a steady-state value of 0.43 after the first ∼20 HfO_2 ALEt cycles in the nucleation regime. This ΔM_{Sn}/MCPC ratio will be used to determine the stoichiometry of the ALEt surface reactions. The standard deviations on the ΔM_{Sn}/MCPC ratio was <0.005.

Figure 5 examines the self-limiting nature of the $Sn(acac)_2$ and HF reactions during HfO_2 ALEt at 200°C. These MCPC values were measured versus different reactant exposure times. Figure 5a shows

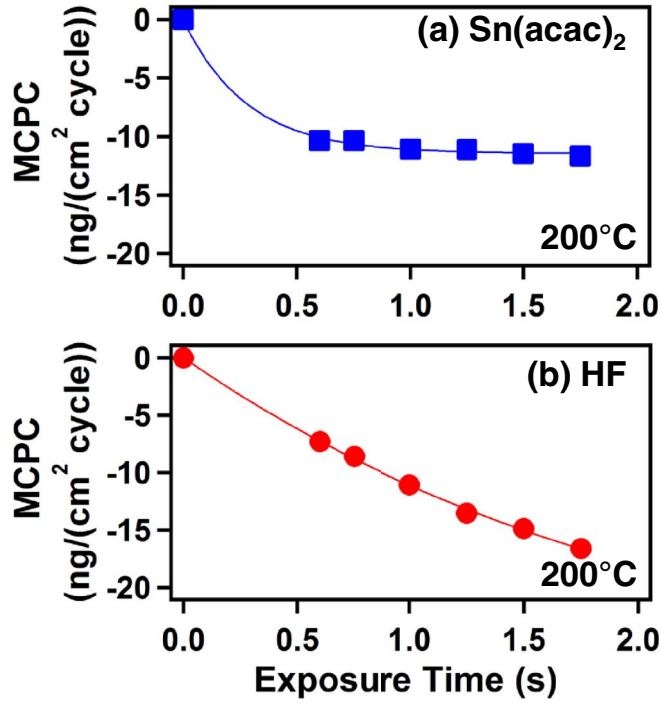

Figure 5. Mass change per cycle (MCPC) versus exposure time for (a) $Sn(acac)_2$ and (b) HF.

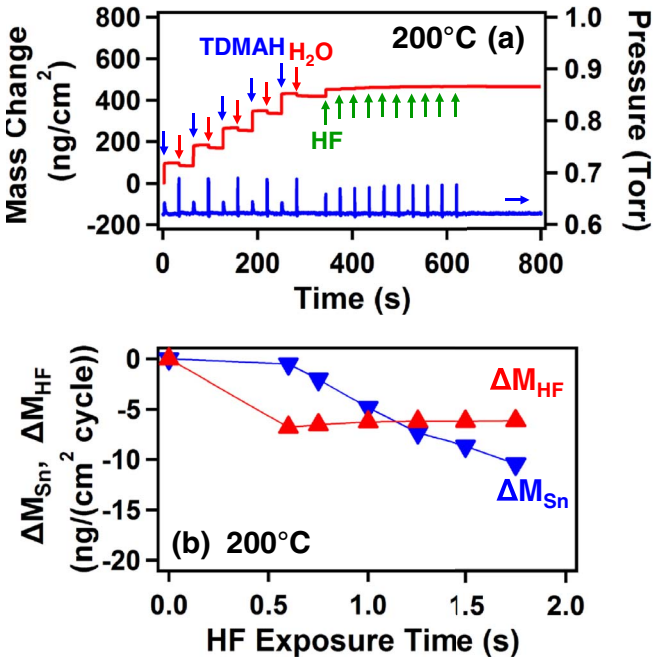

Figure 6. (a) Mass change versus time during five cycles of HfO_2 ALD and then ten HF exposures on the HfO_2 ALD film. (b) ΔM_{Sn} and ΔM_{HF} during HfO_2 ALEt for a $Sn(acac)_2$ exposure of 1.0 s and variable HF exposures.

the self-limiting behavior of the $Sn(acac)_2$ reaction using different $Sn(acac)_2$ exposure times with a single 1.0 s exposure of HF. A constant N_2 purge of 30 s was used after each exposure. This reaction sequence can be denoted as x-30-1-30. The MCPC versus $Sn(acac)_2$ exposure time decreases quickly and levels off at MCPC $= -11$ ng/(cm^2 cycle).

Figure 5b examines the self-limiting behavior of the HF reaction using different HF exposure times with a single 1.0 s exposure of $Sn(acac)_2$. This reaction sequence can be denoted as 1-30-x-30. The MCPC versus HF exposure time decreases and does not level off after longer HF exposure times. The HF reaction does not appear to be self-limiting versus HF exposure. The lack of self-limiting behavior for the HF exposure may indicate that the HF reaction has not reached saturation. Much larger HF exposures may be necessary to complete the surface reaction.

Another possibility is that the larger HF exposures lead to larger HF background pressures and longer HF residence times in the reactor. If some HF residual pressure remains during the $Sn(acac)_2$ exposure, then the HfO_2 substrate can be continuously etched with HF and $Sn(acac)_2$ by chemical vapor etching (CVE). CVE is the reverse of chemical vapor deposition (CVD) and occurs when the two precursors required for ALEt are present at the same time.[39]

Additional experiments were performed to understand the lack of self-limiting behavior for the HF exposure. Figure 6a shows five cycles of HfO_2 ALD followed by ten individual HF exposures at 200°C. The first two HF exposures display a mass gain of $\Delta M_{HF} = 37.8$ ng/cm^2. Subsequent HF exposures display no additional mass change. These results indicate that the HF reaction has reached saturation. This behavior is consistent with the self-limiting adsorption of HF on HfO_2. In addition, HF does not spontaneously etch HfO_2.

Figure 6b shows the ΔM_{Sn} and ΔM_{HF} values for variable HF exposure times with a $Sn(acac)_2$ exposure time of 1.0 s. The ΔM_{HF} values are fairly constant at approximately -6 ng/(cm^2 cycle). This behavior indicates that the ΔM_{HF} values are not responsible for the lack of self-limiting behavior observed in Figure 5b. In contrast, the ΔM_{Sn} values increase progressively with HF exposure time for a fixed $Sn(acac)_2$ exposure time of 1.0 s. This increasing mass loss during the $Sn(acac)_2$ exposure is attributed to HfO_2 CVE caused by the presence of both HF and $Sn(acac)_2$. At longer HF exposure times, more HF residual pressure is believed to be present during the $Sn(acac)_2$ exposure. This HF residual pressure together with the fixed $Sn(acac)_2$ exposure time of 1.0 s leads to HfO_2 CVE.

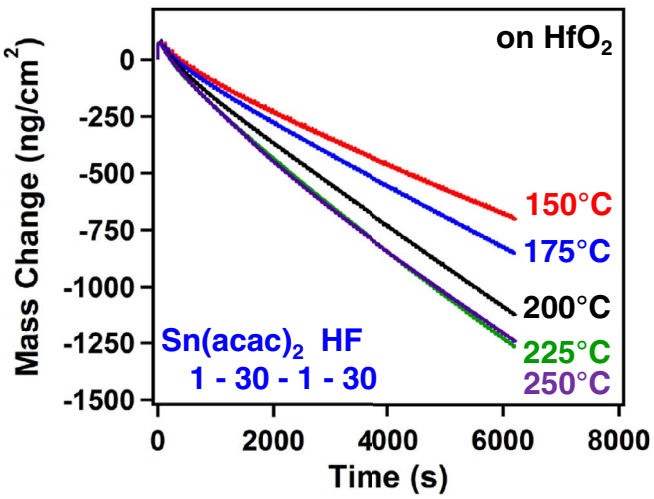

Figure 7. Mass change versus time for HfO_2 ALEt using sequential $Sn(acac)_2$ and HF exposures at 150, 175, 200, 225 and 250°C.

Additional experiments performed at longer purge times than 30 s after the HF exposures did lead to more self-limiting behavior. However, the MCPC continued to increase versus HF exposure time. HF is difficult to purge completely after long HF exposures. The results in Figure 5b should be self-limiting with effective HF purging after HF exposures.

Figure 7 displays the mass change during 100 HfO_2 ALEt cycles using sequential $Sn(acac)_2$ and HF reactions at 150°C, 175°C, 200°C, 225°C, and 250°C. The initial HfO_2 films were grown before HfO_2 ALEt at the same temperatures. These HfO_2 films were deposited by 100 cycles of HfO_2 ALD using TDMAH and H_2O with a sequence of 1-20-1-20. Using the same reaction conditions as employed for the results in Figures 2 and 3, one HfO_2 ALEt cycle consisted of a $Sn(acac)_2$ exposure of 1.0 s, a N_2 purge of 30 s, a HF exposure of 1.0 s, and a second N_2 purge of 30 s.

The HfO_2 ALEt mass changes are linear for all temperatures. The MCPC was determined at steady state after the first 20 HfO_2 ALEt cycles. The MCPC increased at higher temperatures. The MCPC was -6.7, -8.3, -11.1, -11.9, and -11.2 ng/(cm^2 cycle) at 150, 175, 200, 225, and 250°C, respectively. These MCPCs correspond to etch rates of 0.070, 0.087, 0.116, 0.124, and 0.117 Å/cycle at 150, 175, 200, 225 and 250°C, respectively. These etch rates in Å/cycle are based on the HfO_2 ALD film density of 9.6 g/cm^3. The MCPC values are essentially equivalent at 200, 225 and 250°C. The differences in the mass change after 100 cycles for these temperatures are determined mostly by the mass changes in the nucleation regime during the first 20 HfO_2 ALEt cycles.

The ΔM_{Sn}, ΔM_{HF}, and MCPC values at the various reaction temperatures are shown in Figure 8. All HfO_2 ALEt reactions were performed using a reaction sequence of 1-30-1-30 on initial HfO_2 films. Figure 8a shows that ΔM_{Sn} displays a slight mass gain at 150°C and progressively larger mass losses at higher temperatures. In contrast, ΔM_{HF} displays mass losses over the entire temperature range. The mass losses are slightly less at higher temperatures.

Figure 8b reveals that the MCPC increases with temperature between 150 and 200°C. The MCPC values are nearly equivalent at 200, 225 and 250°C. The MCPC in Figure 8b correlates with ΔM_{Sn} in Figure 8a. This correspondence indicates that the mass change during the $Sn(acac)_2$ reaction is primarily responsible for the temperature dependence of the mass loss during HfO_2 ALEt. The ΔM_{Sn}, ΔM_{HF}, MCPC and ΔM_{sn}/MCPC values at the different reaction temperatures are summarized in Table I. Based on previous results for Al_2O_3 ALEt,[24,40] the temperature dependence of the MCPC values is believed to be dependent on the amount of acetylacetonate surface species remaining after the $Sn(acac)_2$ and HF exposures.

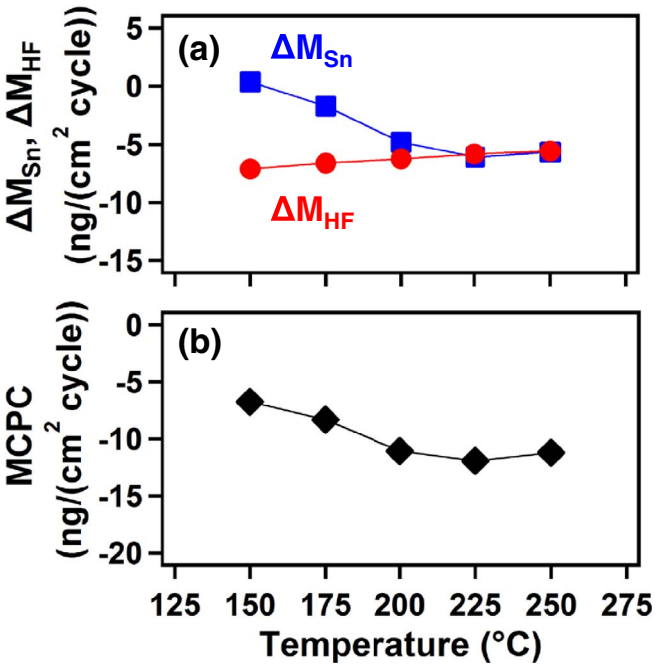

Figure 8. Temperature dependence of (a) ΔM_{Sn} and ΔM_{HF} and (b) MCPC for HfO_2 ALEt.

XRR, XPS and SE measurements.— Ex situ XRR studies also examined HfO_2 ALEt. These XRR experiments employed HfO_2 ALD films with a thickness of 144 Å that were grown on Si(100) wafers. These HfO_2 ALD films were deposited using 150 cycles of TDMAH and H_2O at 200°C with a reaction sequence of 1-20-1-20. Figure 9 shows XRR scans of the HfO_2 ALD films on the Si wafers versus number of $Sn(acac)_2$ and HF reaction cycles at 200°C. The XRR scans have been displaced from each other for clarity. These XRR scans reveal uniform and smooth HfO_2 films.

Figure 9a displays the XRR scan of the initial HfO_2 ALD film grown on Si(100) wafers. The HfO_2 ALD film thickness of 144 Å can be obtained by fitting the reflected X-ray intensity versus incident angle. Figure 9b, 9c, 9d, and 9e show XRR scans of the etched HfO_2 film after 50, 100, 200, and 400 ALEt cycles at 200°C, respectively. The HfO_2 thicknesses decrease with increasing number of ALEt cycles. This decreasing film thickness leads to the decrease in the modulation of the X-ray intensity versus angle with higher numbers of ALEt cycles.

The etched HfO_2 films are smooth and do not roughen versus HfO_2 ALEt. The XRR measurements yielded a roughness of the initial HfO_2 ALD film of ~6 Å. The surface roughness then decreased to ~3-4 Å after 50, 100, 200, and 400 ALEt cycles. The ALEt process is able to smooth the surface of the initial HfO_2 films. The error in these XRR surface roughness measurements is ~1 Å. The position of the critical angle of all the etched HfO_2 films is also constant. This constant critical angle indicates that there is no change of the film density during the ALEt reactions.

Table I. ΔM_{Sn}, ΔM_{HF}, MCPC, ΔM_{Sn}/MCPC, x, and x(MCPC) for HfO_2 ALEt at different temperatures. ΔM_{Sn}, ΔM_{HF}, MCPC and x(MCPC) are expressed in units of ng/(cm^2 cycle).

Temperature (°C)	MCPC	ΔM_{Sn}	ΔM_{HF}	ΔM_{Sn}/MCPC	x	x(MCPC)
150	−6.7	0.37	−7.1	−0.058	1.1	−7.6
175	−8.3	−1.7	−6.6	0.20	0.90	−7.4
200	−11.1	−4.8	−6.3	0.43	0.69	−7.7
225	−11.9	−6.1	−5.8	0.51	0.62	−7.4
250	−11.2	−5.6	−5.6	0.50	0.63	−7.0

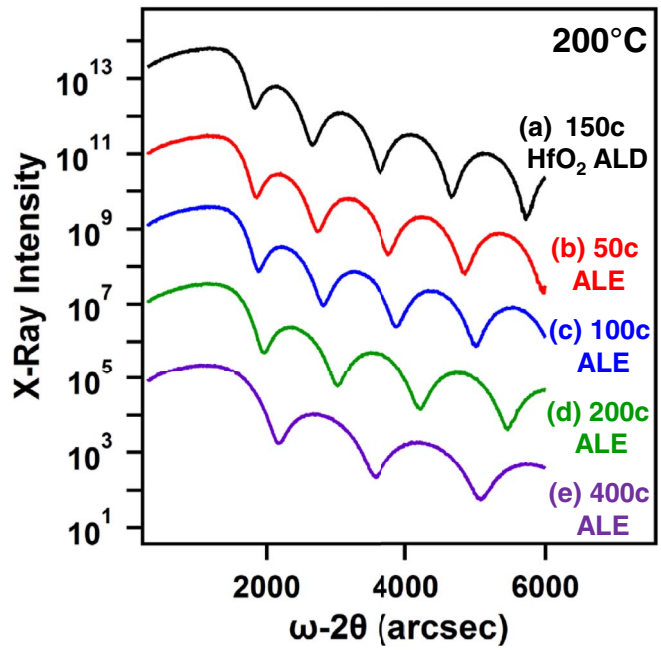

Figure 9. X-ray reflectivity scans showing X-ray intensity versus incident angle for HfO_2 films on Si(100). (a) Initial HfO_2 film grown using 150 HfO_2 ALD cycles; and HfO_2 films after various numbers of HfO_2 ALEt cycles: (b) 50 cycles, (c) 100 cycles, (d) 200 cycles and (e) 400 cycles.

Figure 10 shows the XRR measurements of the initial HfO_2 film thickness and the HfO_2 film thicknesses after 50, 100, 200, and 400 ALEt cycles at 200°C. For the HfO_2 films with an initial thickness of 144 Å in Figure 10a, the film thickness versus number of ALEt cycles is linear and yields an etch rate of 0.11 Å/cycle. The SE measurements on these same samples yield an etch rate of 0.11 Å/cycle with an initial HfO_2 ALD film thickness of 143 Å. The initial thickness of the HfO_2 film was not used to obtain the etch rate because of the mass gain on the first cycle and the nucleation regime that occurs during first 20 ALEt cycles. The SE analysis also determined a refractive index of n = 2.07 for the HfO_2 film at a wavelength of 589 nm. This refractive

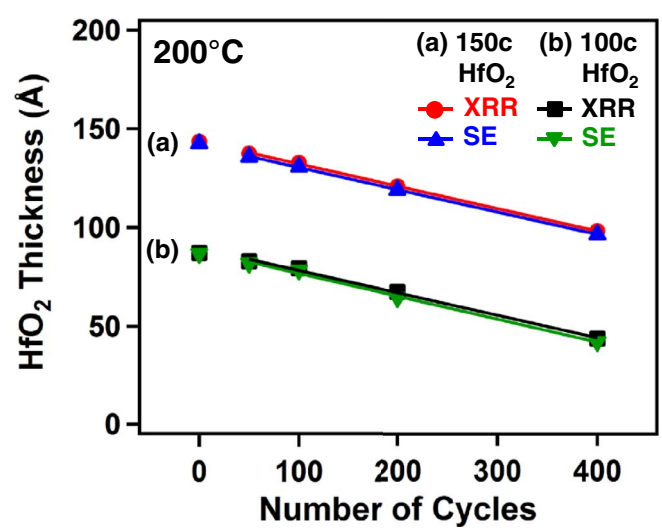

Figure 10. X-ray reflectivity (XRR) and spectroscopic ellipsometry (SE) measurements of HfO_2 film thickness versus number of HfO_2 ALEt cycles for initial HfO_2 ALD films grown using (a) 150 HfO_2 ALD cycles and (b) 100 HfO_2 ALD cycles.

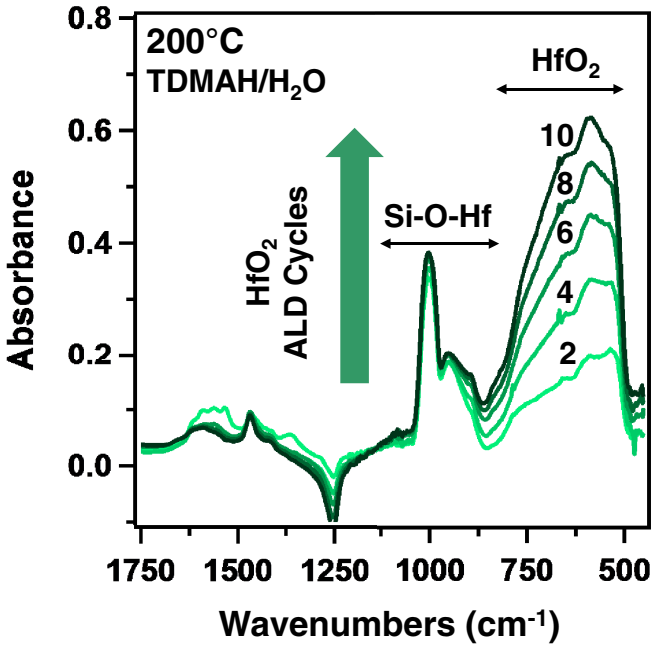

Figure 11. Absolute infrared absorbance showing the growth of Hf-O stretching vibrations in bulk HfO_2 versus number of HfO_2 ALD cycles at 200°C. These FTIR spectra were referenced to the initial SiO_2 particles.

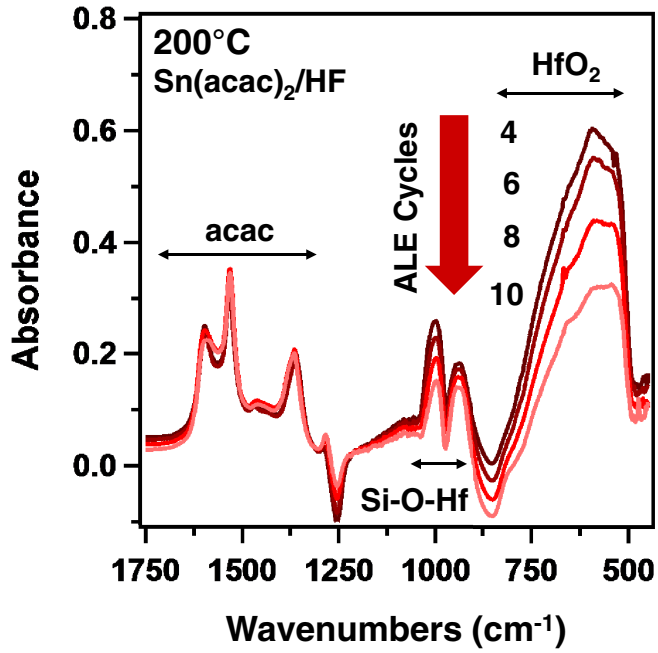

Figure 12. Absolute infrared absorbance showing the loss of Hf-O stretching vibration in bulk HfO_2 versus number of HfO_2 ALEt cycles at 200°C. These FTIR spectra were referenced to the initial SiO_2 particles.

index for the HfO_2 film remained at n = 2.07-2.09 after 50, 100, 200, and 400 ALEt cycles.

XRR measurements were also performed on HfO_2 ALD films with a thickness of 87 Å that were grown on Si(100) wafers. These HfO_2 ALD films were deposited at 200°C using 100 cycles of TDMAH and H_2O with a reaction sequence of 1-20-1-20. Figure 10b displays the film thickness versus number of $Sn(acac)_2$ and HF reaction cycles at 200°C. The XRR measurements yield an HfO_2 ALEt etch rate of 0.11 Å/cycle. The SE measurements also yield an etch rate of 0.12 Å/cycle with an initial HfO_2 ALD film thickness of 87 Å. The initial thickness of the HfO_2 film is again not employed to determine the etch rate because of the mass gain that occurs on the first ALEt cycle and the nucleation regime that occurs during the first 20 ALEt cycles.

X-ray photoelectron spectroscopy (XPS) analysis was used to determine the elements on the HfO_2 film after HfO_2 ALEt. The XPS analysis measured Sn $3d_{5/2}$ XPS signals of 0.47-0.61 at% and F 1s XPS signals of 4.0-4.1 at% after 200 or 400 Al_2O_3 ALEt cycles after the HF exposure. These XPS signals are consistent with residual $Sn(acac)_2$ adsorption products and the formation of HfF_4 or HfF_x surface species. The Sn and F XPS signals were removed to below the XPS detection limit after Ar ion sputtering for 2 minutes. This sputtering time also removes adventitious carbon from the surface.

FTIR Spectroscopy measurements.— In situ FTIR spectra of HfO_2 ALD films grown using 10 cycles of TDMAH and H_2O at 200°C are shown in Figure 11. These FTIR spectra are difference spectra referenced to the initial SiO_2 nanoparticle substrate. The prominent absorbance feature between 500–800 cm^{-1} is attributed to the Hf-O stretching vibrations in bulk HfO_2.[41,42] The absorbance of the Hf-O stretching vibrations in amorphous HfO_2 is broad and ranges from ~200-750 cm^{-1}.[41–43] The breadth of this expected absorbance feature is not observed in Figure 11. The strong absorption from the SiO_2 nanoparticles at ≤500 cm^{-1} obscures the infrared absorbance of the Hf-O stretching vibrations at ≤500 cm^{-1}.

The infrared absorbance of the Hf-O stretching vibration between 500–800 cm^{-1} increases progressively versus number of HfO_2 ALD cycles. In addition to these Hf-O vibrational features, a negative absorption feature appears in Figure 11 at ~1250 cm^{-1} along with a positive absorption feature at ~1000 cm^{-1}. The negative absorption feature at ~1250 cm^{-1} is assigned to the loss of absorbance from Si-O stretching vibrations in the SiO_2 substrate.[44] The positive absorption feature at ~1000 cm^{-1} is attributed to the gain of absorbance from Si-O-Hf stretching vibrations in hafnium silicate.[41,44,45] The hafnium silicate forms almost entirely during the first two HfO_2 ALD cycles on the SiO_2 nanoparticles at 200°C.

Figure 12 shows the FTIR spectra after 4, 6, 8, and 10 ALEt cycles at 200°C. These spectra were recorded after the $Sn(acac)_2$ exposures. Decreasing absorbance for the Hf-O stretching vibration at 500–800 cm^{-1} versus ALEt cycles is consistent with HfO_2 etching. There is also a corresponding decrease in absorbance of the Si-O-Hf vibrations in hafnium silicate at ~1000 cm^{-1}. Infrared absorbance for the $Sn(acac)_2$ adsorption products is also observed in Figure 12 in the range between 1250–1750 cm^{-1}. These vibrational features are derived from the acetylacetonate (acac) constituents.[46,47] These features are consistent with either $Sn(acac)_2^*$, $SnF(acac)^*$ or $acac^*$ adsorbed on the HfO_2 substrate.

Nucleation behavior and proposed HfF_4 formation.— Figure 13 displays an enlargement of the mass changes from Figure 7 during the first two ALEt cycles on HfO_2 films. The first $Sn(acac)_2$ exposure shows mass gains of ΔM_{Sn} = 68–72 ng/cm^2 at 150–250°C resulting from adsorption products of $Sn(acac)_2$ such as $Sn(acac)^*$ and $acacH^*$. To estimate the coverage of $Sn(acac)_2^*$ species on the surface, the sites on the HfO_2 surface can be approximated using the HfO_2 density of 9.6 g/cm^3. This mass density is equivalent to a number density of $\rho = 2.7 \times 10^{22}$ "HfO_2 units"/cm^3. This number density yields an estimate for the number of "HfO_2 units" on the HfO_2 surface of $\rho^{2/3} = 9.10 \times 10^{14}$ "HfO_2 units"/cm^2 assuming a square lattice. This coverage of "HfO_2 units" represents an HfO_2 mass of 320 ng/cm^2.

The coverage of $Sn(acac)_2^*$ can then be approximated based on the mass gain of 72 ng/cm^2. This mass gain is equivalent to 1.37×10^{14} $Sn(acac)_2$ molecules/cm^2. The normalized coverage of $Sn(acac)_2^*$ species relative to "HfO_2 units" on the surface is 1.37×10^{14} $Sn(acac)_2$ molecules/cm^2/9.10×10^{14} "HfO_2 units"/cm^2 = 0.15 $Sn(acac)_2$ species/HfO_2 unit. This coverage is reasonable given that $Sn(acac)_2$ may dissociate into $Sn(acac)^*$ and $acacH^*$. In addition, the acac ligand is bulky and expected to occupy more than one "HfO_2 unit" on the HfO_2 surface.

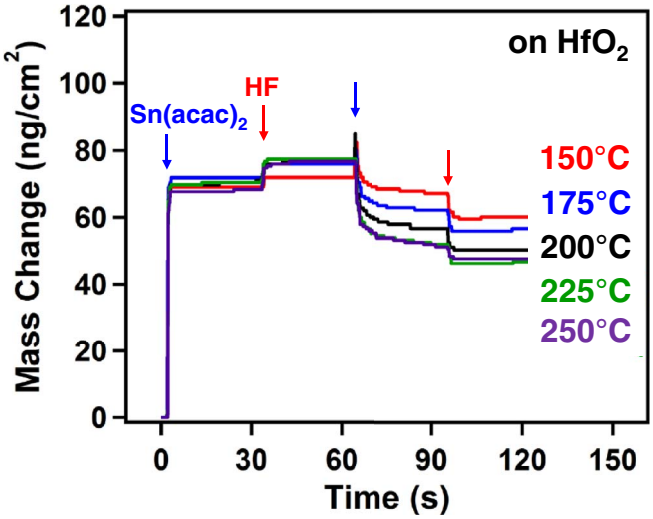

Figure 13. Expansion of first two ALEt cycles in Figure 6 showing the individual mass changes during the sequential $Sn(acac)_2$ and HF exposures at 150, 175, 200, 225 and 250°C.

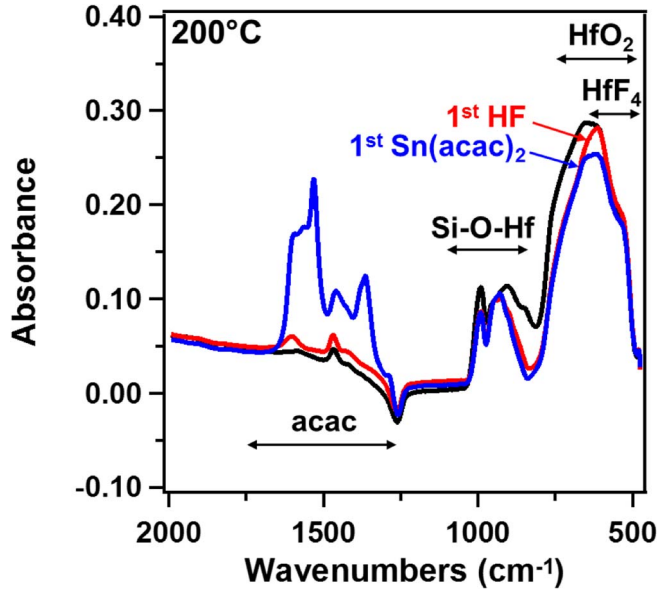

Figure 14. Absolute infrared absorbance showing the Hf-O stretching vibrations in bulk HfO_2 and the acac vibrational features for the first HF and $Sn(acac)_2$ exposures at 200°C. These FTIR spectra were referenced to the initial SiO_2 nanoparticles.

The first HF exposure on the surface previously exposed to $Sn(acac)_2$ shows mass gains of $\Delta M_{HF} = 3$–8 ng/cm^2 at 150–250°C. These mass gains may be affected by the loss of $Sn(acac)_2$ adsorption products. The mass gains following HF exposures on an initial HfO_2 film can be used to estimate the coverage of HF or HF reaction products. A mass gain of 37.8 ng/cm^2 is observed after HF exposures on an initial HfO_2 film at 200°C in Figure 6a. Assuming that HF is the adsorption product, this mass gain is equivalent to 1.14×10^{15} HF molecules/cm^2. The normalized coverage of HF species relative to "HfO_2 units" on the surface is 1.14×10^{15} HF molecules/cm^2/9.10×10^{14} "HfO_2 units"/cm^2 = 1.25 HF/HfO_2 unit.

The HF may also react with the HfO_2 substrate by the reaction: $HfO_2 + 4HF \rightarrow HfF_4 + 2H_2O$. This reaction is predicted to be spontaneous over the temperature range from 150–250°C. The Gibbs free energy changes are negative and decrease slightly in absolute magnitude from $\Delta G = -22$ kcal at 150°C to $\Delta G = -16$ kcal at 250°C.[38] Assuming that HfF_4 is the reaction product, the mass gain of 37.8 ng/cm^2 on an initial HfO_2 film at 200°C is equivalent to a HfF_4 coverage of 5.17×10^{14} HfF_4 molecules/cm^2. The normalized coverage of HfF_4 relative to "HfO_2 units" on the surface is 5.17×10^{14} HfF_4 molecules/cm^2/9.10×10^{14} "HfO_2 units"/cm^2 = 0.57 HfF_4/HfO_2 unit.

Assuming either HF or HfF_4 products, the estimated coverages after the HF exposure are comparable with the number of "HfO_2 units" on the HfO_2 substrate. These coverages are consistent with the rapid and self-limiting fluorination of the HfO_2 surface. In contrast, slow fluorination kinetics of bulk HfO_2 were observed during HF exposures.[48] Thermogravimetric studies showed that bulk HfO_2 did not begin fluorination under HF exposure until >350°C.[48] In addition, HfF_4 was not observed as a product by X-ray diffraction analysis until higher temperatures between 450–580°C.[48] The fluorination of the HfO_2 surface occurs much more readily than the fluorination of bulk HfO_2 substrates.

After the HF exposure, the next $Sn(acac)_2$ exposure reacts with the HfF_4 or HF adlayer on the HfO_2 substrate. Figure 13 shows that mass losses begin with this second $Sn(acac)_2$ exposure and continue with the subsequent HF exposure. Except for the first ALEt cycle shown in Figure 13, all subsequent $Sn(acac)_2$ and HF exposures lead to mass loss resulting from the etching of the HfO_2 film.

The nucleation of the HfO_2 ALEt process was also observed by the FTIR studies. Figure 14 shows FTIR spectra during the first HfO_2 ALEt cycle that are referenced to the starting SiO_2 substrate. For these FTIR spectra, HF was exposed first to the initial HfO_2 film to monitor the surface fluorination to form HfF_4 or HfF_x surface species.

With the first HF exposure, a portion of the Hf-O absorbance feature decreases between 625–800 cm^{-1}. There is also another absorbance decrease between ~800-900 cm^{-1}. These changes may correspond with the conversion of Hf-O stretching vibrations to Hf-F stretching vibrations.

The infrared absorbance between 500–650 cm^{-1} decreases after the first $Sn(acac)_2$ exposure. This decrease is attributed to the removal of HfF_4 or HfF_x surface species. For an HfF_4 adlayer, this removal may occur by the reaction $HfF_4 + 4Sn(acac)_2 \rightarrow Hf(acac)_4 + 4SnF(acac)$. $Sn(acac)_2$ may also adsorb on the thin HfO_2 film and perturb the Hf-O vibrational modes. In addition, pronounced vibrational features associated with acac species on the HfO_2 substrate at 1250–1750 cm^{-1} are observed in Figure 14 after the $Sn(acac)_2$ exposure.

Because the loss in absorbance from HfO_2 and the gain in absorbance from HfF_4 or HfF_x surface species occur in the same frequency range, difference FTIR spectra were examined during the first HF and first $Sn(acac)_2$ exposures on the initial HfO_2 film to distinguish the HfF_4 or HfF_x surface species produced by the first HF exposure. Figure 15a shows the difference spectrum after the first HF exposure. The first HF exposure produces a gain in absorbance between 500–650 cm^{-1} and a loss in absorbance between 650–925 cm^{-1}. The reference spectrum for this FTIR spectrum was the initial HfO_2 film on the SiO_2 nanoparticles. The loss of absorbance between 650–925 cm^{-1} and the gain in absorbance between 500–650 cm^{-1} is attributed to the conversion of HfO_2 to HfF_4 or HfF_x surface species.

Figure 15a also shows that the subsequent $Sn(acac)_2$ exposure removes the absorbance feature associated with the HfF_4 or HfF_x surface species. The reference spectrum for this FTIR spectrum was the previous FTIR spectrum recorded after the HF exposure. This loss of absorbance is expected from the $Sn(acac)_2$ reaction with the HfF_4 or HfF_x surface species. There is also only a small absorbance loss at 650–925 cm^{-1} associated with the higher frequency portion of the absorbance for the Hf-O stretching vibration. The $Sn(acac)_2$ removes the HfF_4 or HfF_x surface species without significantly perturbing the underlying HfO_2 film. For comparison, Figure 15b displays the absorbance loss expected after the removal of an HfO_2 ALD film that was grown using ten HfO_2 ALD cycles.

The absorbance feature between 500–650 cm^{-1} that is centered at ~585 cm^{-1} is attributed to HfF_4 or HfF_x surface species. The frequency of this absorbance feature is slightly lower than the expected frequency of 645–650 cm^{-1} for Hf-F stretching vibrations

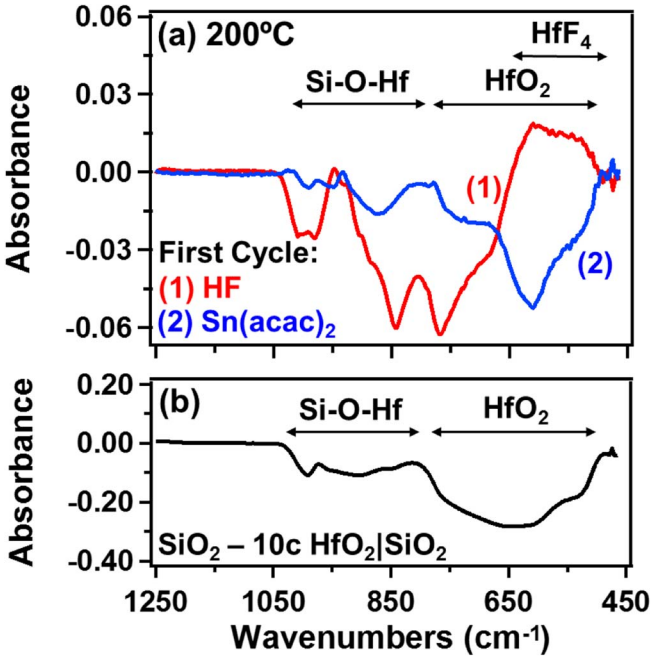

Figure 15. (a) 1. Difference spectrum after HF exposure on an initial HfO_2 film. The reference spectrum was the initial HfO_2 film on the SiO_2 nanoparticles. 2. Difference spectrum after the subsequent $Sn(acac)_2$ exposure. The reference spectrum was the previous FTIR spectrum after the HF exposure. (b) Difference spectrum after removal of 10 cycles of HfO_2 ALD from the SiO_2 nanoparticles. The reference spectrum was the FTIR spectrum after 10 cycles of HfO_2 ALD on the SiO_2 nanoparticles.

in HfF_4.[49,50] To determine the Hf-F stretching vibrational frequency in ultrathin HfF_4 films, HfF_4 ALD films were grown on a thin HfO_2 ALD film on SiO_2 nanoparticles using TDMAH and HF. The FTIR spectra versus number of HfF_4 ALD cycles are displayed in Figure 16. These FTIR spectra are referenced to the initial HfO_2 film on the SiO_2 nanoparticles.

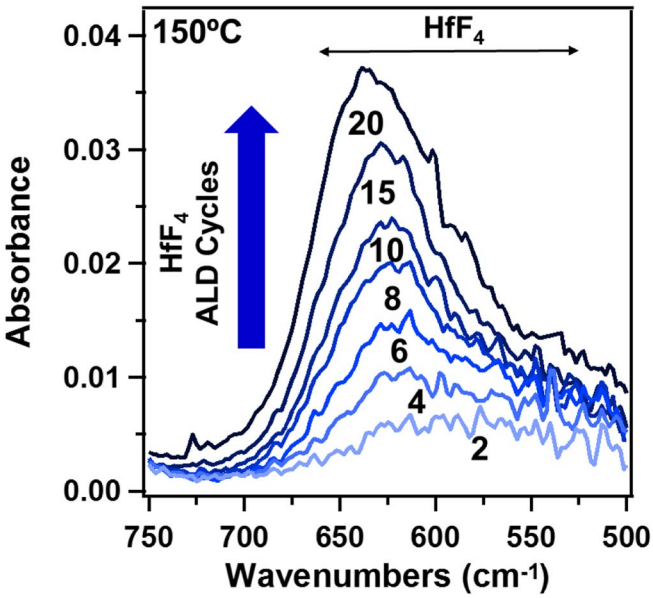

Figure 16. Absolute infrared absorbance showing the growth of Hf-F stretching vibrations in HfF_4 films versus number of HfF_4 ALD cycles at 150°C after the HF exposures. These FTIR spectra are referenced to the initial HfO_2 film on the SiO_2 nanoparticles.

The initial HfF_4 ALD film after two HfF_4 ALD cycles displays increased absorbance in a broad peak centered at ~585 cm^{-1}. The absorbance from these Hf-F stretching vibrations then shifts to higher frequencies with increasing number of HfF_4 ALD cycles. After ~20 HfF_4 ALD cycles, the absorbance peak shifts to ~640 cm^{-1}. This frequency is very close to the frequency of 645–650 cm^{-1} for the Hf-F stretching vibrations in HfF_4.[49,50] These results argue that the absorbance feature in Figure 15a between 500–650 cm^{-1} that is centered at ~585 cm^{-1} is derived from HfF_4 or HfF_x surface species. The Hf-F stretching vibration has a lower frequency in HfF_x surface species or in ultrathin HfF_4 films.

Proposed HfO_2 ALEt reactions.— Figure 17 shows the schematic for the proposed HfO_2 ALEt surface chemistry. This possible picture for HfO_2 ALEt is derived from the mass changes during the $Sn(acac)_2$ and HF exposures as determined by the QCM measurements and the vibrational absorbances observed by the FTIR spectroscopy analysis. This scheme includes only surface species that change during the $Sn(acac)_2$ and HF exposures. This scheme also assumes that the HF reaction produces HfF_4 on the HfO_2 film.

During the $Sn(acac)_2$ reaction (A), $Sn(acac)_2$ reacts with the HfF_4 layer on the HfO_2 substrate to form volatile SnF(acac) and $Hf(acac)_4$ reaction products and SnF(acac)* surface species. After the HfF_4 layer is lost resulting from $Hf(acac)_4$ and SnF(acac) product formation, there may be a strong interaction between SnF(acac)* surface species and the underlying HfO_2 substrate. This interaction may lead to some SnF(acac)* species adsorbed to the HfO_2 substrate.

During the HF reaction (B), HF reacts with some of the SnF(acac)* surface species and the underlying HfO_2 surface to form a HfF_4 layer. In addition, HF also provides hydrogen to form H_2O as a reaction product. This reaction removes the oxygen in HfO_2. The HfF_4 layer is then ready for the next $Sn(acac)_2$ reaction.

The overall proposed reaction can be expressed as:

$$HfO_2 + 4HF + 4Sn(acac)_2 \rightarrow Hf(acac)_4 + 4SnF(acac) + 2H_2O \quad [1]$$

This overall reaction can be divided into the $Sn(acac)_2$ and HF reactions:

$$\text{(A)}\ HfO_2|HfF_4^* + 4Sn(acac)_2 \rightarrow HfO_2|xSnF(acac)^* + Hf(acac)_4 + (4-x)\,SnF(acac) \quad [2]$$

$$\text{(B)}\ HfO_2|xSnF(acac)^* + 4HF \rightarrow HfF_4^* + xSnF(acac) + 2H_2O \quad [3]$$

These reactions include only the species that change during the $Sn(acac)_2$ and HF exposures. The asterisks indicate the surface species and the vertical lines are used to separate the various surface species. Note that HfF_4 is the key reaction intermediate. The production of all the $Hf(acac)_4$ is assumed to occur during reaction (A). $Hf(acac)_4$ is a stable metal β-diketonate with a vapor pressure of ~0.1 Torr at 150°C.[51,52]

The HfO_2 shown in Equations 2 and 3 is the amount of HfO_2 that is etched in one HfO_2 ALEt cycle. x quantifies the coverage of SnF(acac)* on the surface after the $Sn(acac)_2$ exposures relative to the amount of HfO_2 that is etched in one HfO_2 ALEt cycle. x can be determined from the ΔM_{Sn}/MCPC ratio using the equation:

$$x = (254.5 - 210.5(\Delta M_{Sn}/MCPC))/236.8 \quad [4]$$

where 254.5, 210.5 and 236.8 are the molecular weights for HfF_4, HfO_2 and SnF(acac), respectively. The x values are 1.1, 0.90, 0.69, 0.62, and 0.63 at 150, 175, 200, 225 and 250°C, respectively. Table I lists all the x and MCPC values.

x defines the SnF(acac)* species after the $Sn(acac)_2$ exposures relative to the amount of HfO_2 that is etched in one HfO_2 ALEt cycle. Consequently, the product x(MCPC) provides a measure of the SnF(acac)* surface species after the $Sn(acac)_2$ exposures. The x(MCPC) values are included in Table I. These x(MCPC) values are fairly constant at all the temperatures. This behavior indicates that the SnF(acac)* coverage is nearly constant at all the temperatures after

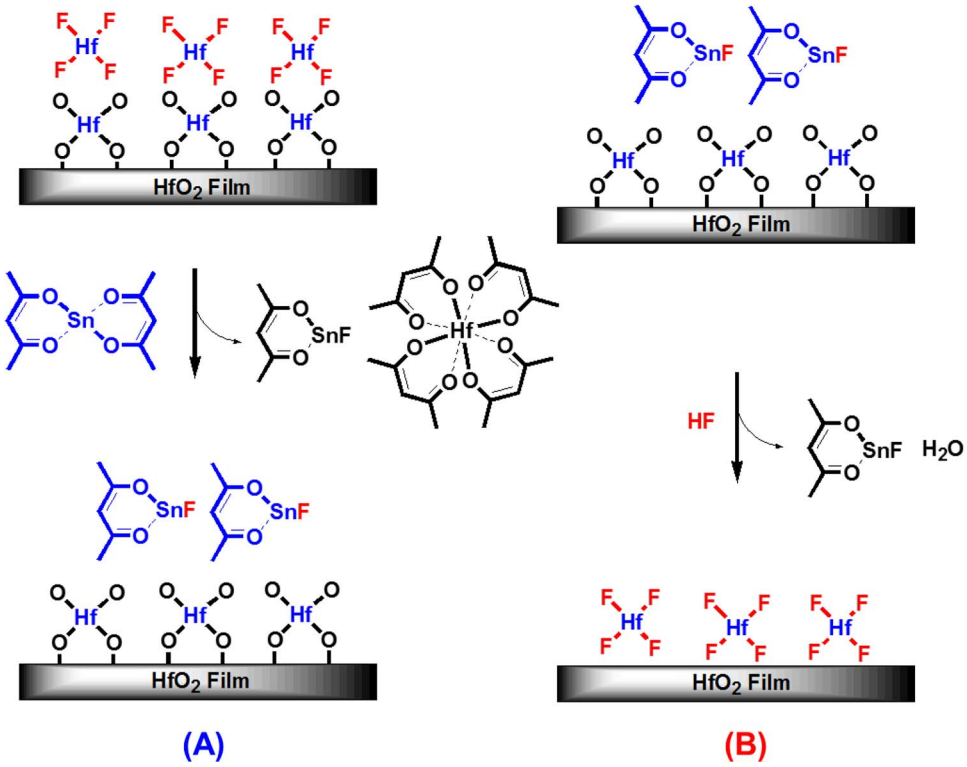

Figure 17. Schematic of proposed surface chemistry for HfO_2 ALEt showing (A) $Sn(acac)_2$ reaction and (B) HF reaction.

the $Sn(acac)_2$ exposures. This coverage may represent a saturated monolayer for SnF(acac)* on the HfO_2 surface.

The proposed reactions for HfO_2 ALEt are similar to the reactions proposed earlier for Al_2O_3 ALEt.[24] Both HfO_2 ALEt and Al_2O_3 ALEt display etching rates that increase at higher temperatures. These temperature dependent etching rates are believed to be correlated inversely with the acetylacetonate coverage remaining on the substrate after the $Sn(acac)_2$ exposure.[24,40] The $Hf(acac)_4$ and $Al(acac)_3$ etching products are both volatile. The vapor pressure of $Hf(acac)_4$ at 150°C is ~0.1 Torr.[51,52] The vapor pressure of $Al(acac)_3$ at 150°C is ~3-4 Torr.[53–55] Both HfO_2 and Al_2O_3 form stable fluorides upon exposure to HF. However, the $Hf(acac)_4$ etching product may become unstable at >100°C.[52] The ΔG for the HF reaction with HfO_2 is also not as favorable as the ΔG for the HF reaction with Al_2O_3.[38] These factors may lead to etching rates for Al_2O_3 ALEt that are higher than the etching rates for HfO_2 ALEt.

Extensions to other materials and advantages of thermal ALEt.— The ALEt of other materials should be possible using sequential, self-limiting thermal reactions with $Sn(acac)_2$ and HF as the reactants.[24] The prospective materials include other metal oxides, metal nitrides, metal phosphides, metal sulfides and metal arsenides.[24] The $Sn(acac)_2$ and HF reactants should be generally useful because $Sn(acac)_2$ can readily react with fluorine to form SnF(acac). Sn-F bond formation is favorable because tin has a high affinity for fluorine.[56] The Sn-F bond enthalpy is 466.5 kJ/mole in the diatomic SnF molecule.[57]

The reaction of $Sn(acac)_2$ with fluorine to form SnF(acac) enables $Sn(acac)_2$ to release an acac ligand to the surface. Metals easily form complexes with acac ligands and have comparable stabilities.[58] The hydrogen from HF can also combine with either oxygen, nitrogen, phosphorous, sulfur or arsenic from the metal oxide, metal nitride, metal phosphide, metal sulfide or metal arsenide to form H_2O, NH_3, PH_3, H_2S or AsH_3, respectively.[24] The ALEt of elemental metals should also be possible by first oxidizing the metal and then etching the resulting metal oxide.[24] Alternatively, elemental metals could be directly fluorinated to form the metal fluoride and then the metal fluoride could be removed by $Sn(acac)_2$.

There are advantages to the thermal ALEt approach compared with ALEt based on halogen adsorption and ion or energetic neutral noble atom bombardment. The thermal ALEt approach avoids any damage to the underlying substrate resulting from high energy ions or energetic neutrals.[59] ALEt based on ion or neutral noble atom bombardment requires line-of-sight to the substrate. This requirement can be used advantageously to minimize undercutting with directional ions or energetic neutral atoms during ALEt. However, this line-of-sight requirement is limited to the small surface areas that are subjected to ion or neutral noble atom bombardment. In contrast, the thermal ALEt approach will be useful for etching larger samples. The thermal ALEt approach will also be important for etching high surface area samples and high aspect ratio structures.

Conclusions

HfO_2 ALEt was demonstrated using $Sn(acac)_2$ and HF as the reactants. The sequential, self-limiting thermal reactions of $Sn(acac)_2$ and HF etched HfO_2 linearly with atomic level precision. HfO_2 ALEt was observed at temperatures from 150–250°C. The $Sn(acac)_2$ reaction was self-limiting versus reactant exposure as revealed by QCM studies. However, the HF reaction was weakly self-limiting presumably because of a high residence time for HF and chemical vapor etching (CVE) caused by the presence of both $Sn(acac)_2$ and HF in the reactor.

The QCM studies measured MCPC values of −6.7, −8.3, −11.1, −11.9, and −11.2 ng/(cm^2 cycle) at 150, 175, 200, 225, and 250°C, respectively. These mass changes per cycle correspond to etch rates of 0.070, 0.087, 0.116, 0.124, and 0.117 Å/cycle at 150, 175, 200, 225 and 250°C, respectively. The linear removal of HfO_2 was confirmed by XRR analysis. The XRR studies measured HfO_2 ALEt etch rates of 0.11 Å/cycle at 200°C. The HfO_2 films also were smoothed by HfO_2 ALEt. HfO_2 ALEt was also observed by FTIR spectroscopy analysis that monitored the loss of absorbance from the Hf-O stretching

vibration of bulk HfO_2 versus number of $Sn(acac)_2$ and HF reaction cycles. FTIR analysis also monitored absorbance features that were consistent with HfF_4 or HfF_x surface species as a reaction intermediate.

The HfO_2 etching is believed to follow the reaction: $HfO_2 + 4Sn(acac)_2 + 4HF \rightarrow Hf(acac)_4 + 4SnF(acac) + 2H_2O$. In the proposed reaction mechanism, HfF_4 or HfF_x is the key reaction intermediate. The $Sn(acac)_2$ reactant donates acac to the HfF_4 or HfF_x adlayer on the HfO_2 substrate to produce $Hf(acac)_4$. The HF reactant forms the HfF_4 or HfF_x reaction intermediate from HfO_2 and allows SnF(acac) and H_2O to leave as reaction products. The ALEt of many other metal oxides besides HfO_2 should also be possible using sequential $Sn(acac)_2$ and HF exposures. This ALEt reaction mechanism should also be applicable for the ALEt of metal nitrides, metal phosphides, metal arsenides and elemental metals.

Acknowledgments

This research was funded by the National Science Foundation (CHE-1306131). Additional personnel support for YL was provided by the Department of Energy through the DOE-BATT program. The authors thank Huaxing Sun for X-ray photoelectron spectroscopy (XPS) analysis of elemental film composition.

References

1. A. Agarwal and M. J. Kushner, *J. Vac. Sci. Technol. A*, **27**, 37 (2009).
2. S. D. Athavale and D. J. Economou, *J. Vac. Sci. Technol. A*, **13**, 966 (1995).
3. S. D. Athavale and D. J. Economou, *J. Vac. Sci. Technol. B*, **14**, 3702 (1996).
4. S. M. George, *Chem. Rev.*, **110**, 111 (2010).
5. M. Leskela and M. Ritala, *Angew. Chem. Int. Ed.*, **42**, 5548 (2003).
6. N. Marchack and J. P. Chang, *J. Phys. D Appl. Phys.*, **44**, 174011 (2011).
7. J. B. Park, W. S. Lim, B. J. Park, I. H. Park, Y. W. Kim, and G. Y. Yeom, *J. Phys. D Appl. Phys.*, **42**, 055202 (2009).
8. N. A. Kubota, D. J. Economou, and S. J. Plimpton, *J. Appl. Phys.*, **83**, 4055 (1998).
9. S. D. Park, D. H. Lee, and G. Y. Yeom, *Electrochem. Solid State Lett.*, **8**, C106 (2005).
10. S. D. Park, W. S. Lim, B. J. Park, H. C. Lee, J. W. Bae, and G. Y. Yeom, *Electrochem. Solid State Lett.*, **11**, H71 (2008).
11. H. Sakaue, S. Iseda, K. Asami, J. Yamamoto, M. Hirose, and Y. Horiike, *Jpn. J. Appl. Phys. 1*, **29**, 2648 (1990).
12. J. Yamamoto, T. Kawasaki, H. Sakaue, S. Shingubara, and Y. Horiike, *Thin Solid Films*, **225**, 124 (1993).
13. T. Sugiyama, T. Matsuura, and J. Murota, *Appl. Surf. Sci.*, **112**, 187 (1997).
14. W. S. Lim, S. D. Park, B. J. Park, and G. Y. Yeom, *Surf. Coat. Tech.*, **202**, 5701 (2008).
15. T. Meguro, M. Hamagaki, S. Modaressi, T. Hara, Y. Aoyagi, M. Ishii, and Y. Yamamoto, *Appl. Phys. Lett.*, **56**, 1552 (1990).
16. T. Meguro, M. Ishii, T. Sugano, K. Gamo, and Y. Aoyagi, *Appl. Surf. Sci.*, **82**, 193 (1994).
17. S. D. Park, C. K. Oh, J. W. Bae, G. Y. Yeom, T. W. Kim, J. I. Song, and J. H. Jang, *Appl. Phys. Lett.*, **89**, 043109 (2006).
18. J. B. Park, W. S. Lim, S. D. Park, Y. J. Park, and G. Y. Yeom, *J. Korean Phys. Soc.*, **54**, 976 (2009).
19. D. Metzler, R. L. Bruce, S. Engelmann, E. A. Joseph, and G. S. Oehrlein, *J. Vac. Sci. Technol. A*, **32**, 020603 (2014).
20. K. S. Min, S. H. Kang, J. K. Kim, Y. I. Jhon, M. S. Jhon, and G. Y. Yeom, *Microelectron. Eng.*, **110**, 457 (2013).
21. Y. Y. Kim, W. S. Lim, J. B. Park, and G. Y. Yeom, *J. Electrochem. Soc.*, **158**, D710 (2011).
22. W. S. Lim, Y. Y. Kim, H. Kim, S. Jang, N. Kwon, B. J. Park, J.-H. Ahn, I. Chung, B. H. Hong, and G. Y. Yeom, *Carbon*, **50**, 429 (2012).
23. E. Vogli, D. Metzler, and G. S. Oehrlein, *Appl. Phys. Lett.*, **102**, 253105 (2013).
24. Y. Lee and S. M. George, *ACS Nano*, **9**, 2061 (2015).
25. J. H. Choi, Y. Mao, and J. P. Chang, *Mater. Sci. Eng., R*, **72**, 97 (2011).
26. J. Robertson, *Eur. Phys. J. Appl. Phys.*, **28**, 265 (2004).
27. M. H. Cho, Y. S. Roh, C. N. Whang, K. Jeong, S. W. Nahm, D. H. Ko, J. H. Lee, N. I. Lee, and K. Fujihara, *Appl. Phys. Lett.*, **81**, 472 (2002).
28. K. Mistry, C. Allen, C. Auth, B. Beattie, D. Bergstrom, M. Bost, M. Brazier, M. Buehler, A. Cappellani, R. Chau, C. H. Choi, G. Ding, K. Fischer, T. Ghani, R. Grover, W. Han, D. Hanken, M. Hatttendorf, J. He, J. Hicks, R. Huessner, D. Ingerly, P. Jain, R. James, L. Jong, S. Joshi, C. Kenyon, K. Kuhn, K. Lee, H. Liu, J. Maiz, B. McIntyre, P. Moon, J. Neirynck, S. Pei, C. Parker, D. Parsons, C. Prasad, L. Pipes, M. Prince, P. Ranade, T. Reynolds, J. Sandford, L. Schifren, J. Sebastian, J. Seiple, D. Simon, S. Sivakumar, P. Smith, C. Thomas, T. Troeger, P. Vandervoorn, S. Williams, and K. Zawadzki, *2007 IEEE International Electron Devices Meeting*, **1-2**, 247 (2007).
29. T. Rudenko, N. Collaert, S. De Gendt, V. Kilchytska, M. Jurczak, and D. Flandre, *Microelectron. Eng.*, **80**, 386 (2005).
30. A. Tsormpatzoglou, D. H. Tassis, C. A. Dimitriadis, M. Mouis, G. Ghibaudo, and N. Collaert, *Semicond. Sci. Technol.*, **24** (2009).
31. J. W. Elam, M. D. Groner, and S. M. George, *Rev Sci Instrum*, **73**, 2981 (2002).
32. S. C. Riha, J. A. Libera, J. W. Elam, and A. B. F. Martinson, *Rev Sci Instrum*, **83**, 094101 (2012).
33. G. A. Olah, M. Nojima, and I. Kerekes, *Synthesis-Stuttgart*, **12**, 779 (1973).
34. R. D. Shannon, R. C. Shannon, O. Medenbach, and R. X. Fischer, *J. Phys. Chem. Ref. Data* **31**, 931 (2002).
35. J. W. DuMont and S. M. George, *Journal of Physical Chemistry C* (In Press).
36. J. D. Ferguson, A. W. Weimer, and S. M. George, *Thin Solid Films*, **371**, 95 (2000).
37. T. H. Ballinger, J. C. S. Wong, and J. T. Yates, *Langmuir*, **8**, 1676 (1992).
38. HSC Chemistry, Version 5.1; Outokumpu Research Oy: Pori, Finland.
39. R. Steger and R. Masel, *Thin Solid Films*, **342**, 221 (1999).
40. Y. Lee, J. W. DuMont, and S. M. George, *Submitted to Chemistry of Materials*.
41. D. A. Neumayer and E. Cartier, *J. Appl. Phys.*, **90**, 1801 (2001).
42. Y. Wang, M. T. Ho, L. V. Goncharova, L. S. Wielunski, S. Rivillon-Amy, Y. J. Chabal, T. Gustafsson, N. Moumen, and M. Boleslawski, *Chem. Mater.*, **19**, 3127 (2007).
43. D. Ceresoli and D. Vanderbilt, *Phys. Rev. B*, **74** (2006).
44. V. Cosnier, M. Olivier, G. Theret, and B. Andre, *J. Vac. Sci. Technol.*, **19**, 2267 (2001).
45. L. Khomenkova, *Physica B*, **453**, 19 (2014).
46. K. Nakamoto, A. E. Martell, and P. J. McCarthy, *J. Am. Chem. Soc.*, **83**, 1272 (1961).
47. S. F. Tayyari and F. Milani-nejad, *Spectrochim. Acta A*, **56**, 2679 (2000).
48. B. M. Vilakazi, O. S. Monnahela, J. B. Wagener, P. A. B. Carstens, and T. Ntsoane, *J. Fluorine Chem.*, **141**, 64 (2012).
49. A. Buechler, D. H. Dugre, and J. B. Berkowitz, *J. Chem. Phys.*, **34**, 2202 (1961).
50. V. N. Bukhmarina, S. L. Dobychin, Y. B. Predtechenskii, and V. G. Shklyarik, *Zhurnal Fizicheskoi Khimii*, **60**, 1775 (1986).
51. N. B. Morozova, K. V. Zherikova, I. A. Baidina, S. V. Sysoev, P. P. Semyannikov, L. V. Yakovkina, T. P. Smirnova, N. V. Gelfond, I. K. Igumenov, G. Carta, and G. Rossetto, *J. Phys. Chem. Solids*, **69**, 673 (2008).
52. K. V. Zherikova, N. B. Morozova, L. N. Zelenina, S. V. Sysoev, T. P. Chusova, and I. K. Igumenov, *J. Therm. Anal. Calorim.*, **92**, 729 (2008).
53. E. W. Berg and J. T. Truemper, *Anal. Chim. Acta*, **32**, 245 (1965).
54. K. J. Eisentraut and R. E. Sievers, *J. Inorg. Nucl. Chem.*, **29**, 1931 (1967).
55. B. D. Fahlman and A. R. Barron, *Adv. Mater. Opt. Electr.*, **10**, 223 (2000).
56. P. F. R. Ewings, P. G. Harrison, and D. E. Fenton, *J Chem Soc Dalton*, 821 (1975).
57. K. Zimbov, J. W. Hastie, and J. L. Margrave, *T Faraday Soc*, **64**, 861 (1968).
58. R. C. Mehrotra, R. Bohra, and D. P. Gaur, *Metal Beta-Diketonates and Allied Derivatives*, p. viii, Academic Press, London (1978).
59. M. M. Hussain, S.-C. Song, J. Barnett, C. Y. Kang, G. Gebara, B. Sassman, and N. Moumen, *IEEE Elect. Device Lett.*, **27**, 972 (2006).